Yao et al. *Zool. Res.* 2026, 47(1): 58−71
https://doi.org/10.24272/j.issn.2095-8137.2025.121
https://cstr.cn/32248.14.zr.2025.121

ZR | Zoological Research

Article Open Access

Dynamic single-nucleus transcriptomic profiling of kidney development in Bamaxiang pigs and wild boar

Tian-Xiong Yao[1,#,*], Yang Zhang[1,#], Xiao-Yun Chen[1], Ting Luo[1], Yang Li[1], Si-Yu Yang[1,*]

[1] *National Key Laboratory for Swine Genetic Improvement and Germplasm Innovation*, *Ministry of Science and Technology of China*, *Jiangxi Agricultural University*, *Nanchang*, *Jiangxi* 330045, *China*

ABSTRACT

Defining developmental periods- and breed-specific cellular features of the porcine kidney is critical for refining donor selection strategies in xenotransplantation. This study utilized single-nucleus RNA sequencing to generate 71 081 high-quality transcriptomes from eight kidneys sampled across three developmental periods—weaning, fattening, and maturity—in Bamaxiang (BMX) and wild boar (WB) breeds. A total of 33 distinct cell types were identified. Proximal tubule (PT), principal (PC), and thick ascending limb (TAL) cells exhibited pronounced transcriptional transitions across developmental periods. PT cells displayed a temporal shift from early development-related functions during the weaning period to metabolic and transport functions during fattening and maturity. Subclustering of PT cells revealed discrete functional subtypes, including a mature WB-specific PT2 cluster enriched in immune function regulation. In PC cells, both breeds expressed a shared PC0 subtype during weaning with signatures of cellular development. The WB-specific PC2 subtype was enriched in thermoregulation pathways, whereas at maturity, the BMX-specific PC0 subtype exhibited transcriptional features associated with oxidative metabolism and the WB-specific PC1 subtype expressed genes involved in glucose metabolism. These findings suggest divergent physiological adaptations to domestication and wild environments. Cell-cell interaction analysis identified the epidermal growth factor (EGF) signaling pathway as the most active across BMX kidney development, with epithelial tubule subtypes engaging in ligand-receptor interactions via ligands, including betacellulin (BTC), EGF, and transforming growth factor-α (TGF-α).

Keywords: Pig kidney; Bamaxiang pig; Wild Boar; Developmental period; Single-nucleus RNA sequencing

INTRODUCTION

The kidney plays an essential role in mammalian physiology by maintaining fluid volume, regulating electrolytes and metabolic waste, and contributing to systemic blood pressure control (Alpern et al., 2012; Guyton & Hall, 2005). These functions undergo dynamic changes across developmental stages, accompanied by shifts in cellular composition and molecular profiles. Such temporal remodeling influences core renal functions, including filtration, osmoregulation, and adaptive stress responses (Gossens & Unsworth, 1972; Márquez et al., 2002; Miao et al., 2021; Rane et al., 1985; Saxen, 1987; Stewart et al., 2019; Velarde et al., 1995; Yao et al., 2025). In addition, genetic background exerts substantial influence over renal architecture and gene expression, with breed-specific variation contributing to physiological divergence (He et al., 2017; Kojima et al., 2022; Lobacz et al., 2012; Timoneda et al., 2013). Divergent environmental exposures and rearing conditions further modulate regulatory capacity, leading to pronounced differences in renal phenotype across domestic and wild lineages (Bolhuis et al., 2006; Collier et al., 1982; He et al., 2017; Johnson et al., 2016; Keuling et al., 2008; Kshirsagar et al., 2022; Russo et al., 1997; Zhang et al., 2025).

As the global burden of renal failure continues to rise (Miao et al., 2024), the demand for transplantation exceeds the availability of donor organs. Among experimental animal models, porcine kidneys have emerged as leading candidates for xenotransplantation due to their anatomical and physiological resemblance to human kidneys (Lunney et al., 2021). Recently, several preclinical trials in the United States and China have achieved successful xenotransplantation of porcine kidneys into living human recipients (Cohen, 2025; Mass General Brigham Communications, 2024; Qin & Zou, 2025), marking a critical milestone in the translation of this approach into clinical practice. With ongoing advancements in genome editing, immunological engineering, and surgical

Received: 09 August 2025; Accepted: 08 September 2025; Online: 09 September 2025

Foundation items: This work was supported by the International Cooperation and Exchange Program of the National Natural Science Foundation of China (32261133531) and China Agriculture Research System (CARS-35)

[#]Authors contributed equally to this work

*Corresponding authors, E-mail: TianxiongYao@hotmail.com; siyuyang1013@163.com

methodology, future research is expected to move toward precision xenotransplantation tailored to recipient-specific requirements.

To support these efforts, the present study systematically characterized the cellular composition and transcriptional features of porcine kidneys across developmental stages in two genetically and environmentally divergent breeds. These foundational data establish a molecular and cellular reference for optimizing donor selection and accelerating the implementation of stage- and breed-informed xenotransplantation strategies.

MATERIALS AND METHODS

Ethical statement

All procedures and experiments involving pigs were approved by the Animal Ethics Committee of Jiangxi Agricultural University (JXAULL-2021-11-018).

Pig kidney tissue collection

Kidney samples were collected from male Bamaxiang (BMX) pigs and wild boars (WB) at three key developmental periods. Both breeds were sourced from the same pig farm in Pingxiang, Jiangxi Province, China. While BMX pigs were conventionally raised, WB were maintained under free-range conditions in mountainous wooded areas, approximating their natural habitat. For BMX pigs, five kidney samples were collected at weaning (postnatal days 30 and 42), fattening (postnatal days 150), and maturity (postnatal days 730 and 774) periods. For WB, three samples were collected at equivalent stages: weaning (postnatal days 42), fattening (postnatal days 150), and maturity (postnatal days 730) (Supplementary Table S1).

Single-nucleus RNA-sequencing (snRNA-seq) sample tissue isolation

Nuclei were isolated using Nuclei EZ Lysis buffer (NUC-101; Sigma-Aldrich, USA), supplemented with protease inhibitor (5892791001; Roche, Germany) and RNase inhibitors (N2615, Promega, USA; AM2696, Life Technologies, USA). Fresh kidney tissue was sectioned into approximately 1 mm-sized pieces and homogenized in 2 mL of ice-cold lysis buffer using a Dounce homogenizer (885302-0002; Kimble Chase, Germany). After homogenization, an additional 2 mL of lysis buffer was added, and the sample was incubated on ice for 5 min. The homogenate was further disrupted using a Dounce homogenizer (Sigma, USA) and gently resuspended by pipetting, followed by an additional 6 min of incubation on ice. To terminate lysis, 2 mL of ice-cold 4% bovine serum albumin (BSA) was added and gently mixed using a Pasteur pipette. Nuclei were pelleted by centrifugation at 300 ×*g* for 5 min at 4°C, resuspended in 2 mL of lysis buffer containing 4% BSA, and incubated on ice for an additional 3 min. Debris was removed using Miltenyi Debris Removal Solution. The nuclei pellet was resuspended and washed in 4 mL of buffer, incubated on ice for 5 min, and centrifuged again. The resulting pellet was resuspended in Nuclei Suspension Buffer (1×phosphate-buffered saline (PBS) supplemented with 0.07% BSA and 0.1% RNase inhibitor), filtered through a 20 μm cell strainer (43-50020-50; pluriSelect, Germany), and quantified using a Countess II Automated Cell Counter (USA). Nuclear concentration was adjusted to 700–1 200 nuclei/μL.

Chromium 10× Genomics library preparation and sequencing

Single-nucleus suspensions were processed using the Chromium 10× Genomics platform following the manufacturer's instructions for the Chromium Single-Cell 3' Kit v.3 (10× Genomics). The cDNA amplification and library construction were carried out according to standard procedures. Sequencing was performed on the Illumina NovaSeq 6000 platform (paired-end, 150 bp reads; USA) by LC-BioTechnology Co. Ltd. (Hangzhou, China).

Processing and quality control of snRNA-seq data

Raw sequencing data were demultiplexed and converted to FASTQ format using Illumina bcl2fastq2 (v.2.20, USA). Cell Ranger (v.7.0.0) (Zheng et al., 2017) was used for sample demultiplexing, barcode processing, and gene expression quantification. Background RNA contamination was removed using the "remove-background" function in CellBender (v.0.3.0) (Fleming et al., 2023). Downstream quality control, dimensionality reduction, and clustering analyses were conducted using Scanpy (v.1.9.2) within the Python environment (v.3.10.8) (Wolf et al., 2018). For each sample, expression matrices were filtered to exclude the following: (1) cells with fewer than 500 genes (650 for WB at postnatal day 730) or more than 6 000 genes (8 000 for WB); (2) cells with more than 30 000 UMIs (50 000 for WB); (3) cells with mitochondrial content > 40%; (4) genes expressed in fewer than three cells; and (5) potential doublet cells predicted by Scrublet (v.0.2.3) (Wolock et al., 2019) with a score >0.10 (Supplementary Table S1).

Data integration and cell type annotation

Filtered gene expression matrices were merged and normalized using the "NormalizeData" function in Seurat (v.4.3.0.1) (Hao et al., 2021). The top 2 000 highly variable genes were selected using the "FindVariableFeatures" function, followed by integration across datasets using the "FindIntegrationAnchors" and "IntegrateData" functions, which mitigated batch effects between breeds. The data were scaled using the "ScaleData" function and subjected to principal component analysis (PCA) using "RunPCA". Uniform Manifold Approximation and Projection (UMAP) dimensionality reduction was performed using the top 30 principal components (PCs) via "RunUMAP". Clustering was executed using the "FindNeighbors" and "FindClusters" functions with resolution set to 0.8. Seven major cell types were annotated, including epithelial cells (EpCs), proliferating epithelial cells (ProlifEpCs), endothelial cells (ECs), immune cells (IMs), fibroblasts (Fibs), smooth muscle cells (SMCs), and glomerular pericytes (GPCs).

For subtyping, EpC populations were extracted from the merged dataset and processed independently. Raw counts were normalized and log-transformed using the "scanpy.pp.normalize_total" and "scanpy.pp.log1p" functions in Python. The top 2 000 highly variable genes were identified using "scanpy.pp.highly_variable", followed by PCA using "scanpy.tl.pca". Harmony (v.0.0.9) (Korsunsky et al., 2019) was used to integrate the data to eliminate inter-breed effects. UMAP projection and clustering were performed using "scanpy.tl.umap" and "scanpy.tl.louvain". Final cluster annotation was based on canonical marker genes curated from public databases (Franzén et al., 2019; Uhlén et al., 2015) and published literature (Balzer et al., 2022; El-Achkar et al., 2021; Lake et al., 2023). Subtype identification for IM

and EC populations followed the same workflow.

Cross-species cell annotation validation

To assess the accuracy of cell type annotation, cross-species label transfer was performed using the "FindTransferAnchors" and "TransferData" functions in Seurat. Pig kidney cells (query) were mapped to annotated human/mouse kidney cell datasets (reference) to establish transcriptomic correspondence. Prediction scores were calculated for each cell and median-averaged within each annotated cluster. Publicly available reference datasets included the 2023 human kidney dataset from Nature (https://cellxgene.cziscience.com/collections/bcb61471-2a44-4d00-a0af-ff085512674c), the 2019 human kidney dataset from Science (https://explore.data.humancellatlas.org/projects/abe1a013-af7a-45ed-8c26-f3793c24a1f4), and the 2021 mouse kidney data from Nature Communications (https://www.ncbi.nlm.nih.gov/geo/query/acc.cgi?acc=GSE157079).

Fluorescent double immunostaining of frozen sections

Frozen kidney sections were pre-incubated at 37°C for 10–20 min to remove residual moisture and improve adherence. Sections were then fixed in fixative solution for 30 min and washed three times in PBS (pH 7.4) on a decolorizing shaker (5 min each). Antigen retrieval was conducted according to the optimized conditions ensuring minimal buffer evaporation. After natural cooling, slides were immersed in PBS (pH 7.4) and washed three times (5 min each). Following gentle drying, a histochemical pen was used to delineate the tissue. Endogenous peroxidase activity was blocked by incubation in 3% hydrogen peroxide at room temperature for 25 min in the dark. Slides were again washed three times in PBS as above. Serum blocking was performed for 30 min at room temperature: 10% goat serum was used for rabbit-derived primary antibodies, while 3% BSA was used for antibodies from other species. After removing the blocking solution, sections were incubated with the prepared primary antibody at 4°C overnight in a humidified chamber. Slides were then washed in PBS as above, gently dried, and incubated with the corresponding horseradish peroxidase (HRP)-labeled secondary antibody for 50 min at room temperature. After another PBS wash cycle (as above), TSA amplification reagent was applied for 10 min in the dark at room temperature, followed by washing three times with TBST (5 min each) on a decolorizing shaker.

For sequential staining, antigen retrieval was repeated using the same buffer. Sections were microwaved for 8 min at medium power and 7 min at medium-low power. After natural cooling, the second primary antibody was applied and incubated overnight at 4°C. The following day, slides were washed in PBS (as above), slightly dried, and incubated with the corresponding fluorescent secondary antibody at room temperature for 50 min in the dark. After another PBS wash cycle (as above), nuclei were counterstained with DAPI for 10 min at room temperature in the dark and washed again in PBS (as above).

To quench autofluorescence, B-type quencher solution was added for 5 min and rinsed under running water for 10 min. This step was omitted when autofluorescence visualization was desired. Finally, sections were sealed using anti-fluorescence quenching mounting medium and imaged using filters appropriate for the following channels: DAPI (excitation 330–380 nm, emission 420 nm), 488 (excitation 465–495 nm, emission 515–555 nm), CY3 (excitation 510–560 nm, emission 590 nm), and CY5 (excitation 608–648 nm, emission 672–712 nm).

Heterogeneous double immunofluorescence staining of paraffin sections

Paraffin-embedded sections were deparaffinized by immersion in three changes of xylene (10 min each), followed by dehydration through a graded ethanol series (5 min each). The sections were then washed in distilled water. Antigen retrieval was carried out under specific conditions, with careful maintenance of buffer volume to prevent evaporation. Slides were not allowed to dry at any point during this process. After retrieval, sections were naturally cooled, washed three times in PBS (pH 7.4) on a decoloring shaker (5 min), and gently dried. Tissue boundaries were outlined using a Liquid Blocker PAP Pen. For serum blocking, 10% donkey serum was used for goat-derived primary antibodies, while 3% BSA was used for antibodies from other sources. Blocking was performed for 30 min at room temperature. Primary antibody mixtures, prepared by combining two antibodies from different host species, were applied to the sections and incubated overnight at 4°C in a humidified chamber, followed by three PBS washes (as above) the next day. Species-appropriate fluorescent secondary antibodies were added and incubated at room temperature for 50 min in the dark. Slides were again washed three times with PBS (as above), followed by nuclear counterstaining with DAPI solution, which was applied to the marked area and incubated at room temperature for 10 min in the dark. To quench tissue autofluorescence, slides were washed three times with PBS (as above), treated with B-type quencher solution for 5 min, and rinsed under running water for 10 min. After staining, slides were mounted using an anti-fade medium and coverslipped. Fluorescence signals were visualized using a fluorescence microscope equipped with the following filter settings: DAPI (excitation 330–380 nm, emission 420 nm), 488 (excitation 465–495 nm, emission 515–555 nm), and CY3 (excitation 510–560 nm, emission 590 nm).

Sequential double immunofluorescence staining of paraffin sections

Paraffin sections were dewaxed by sequential immersion in environmental dewaxing solutions I, II, and III for 10 min each, followed by rehydration through three changes of anhydrous ethanol (I, II, and III) for 5 min each and rinsing in distilled water. Antigen retrieval was performed under specific conditions. Buffer evaporation was minimized during the process, and slides were not allowed to dry. After retrieval, slides were naturally cooled, then washed three times in PBS (pH 7.4) on a decolorizing shaker (5 min each). Following slight drying, tissue boundaries were outlined using a hydrogen peroxide-sealed histochemical pen. Sections were then incubated in 3% hydrogen peroxide at room temperature for 25 min in the dark to block endogenous peroxidase activity. After washing in PBS (as above), serum blocking was performed. Specifically, 10% goat serum was used for rabbit-derived primary antibodies, while 3% BSA was used for antibodies from other sources. Blocking was carried out for 30 min at room temperature.

After removing the blocking solution, the first primary antibody was applied to the circled area. Slides were placed flat in a humidified chamber and incubated overnight at 4°C, then washed in PBS (as above). After gentle drying, the corresponding HRP-labeled secondary antibody was added

and incubated at room temperature for 50 min, followed by another cycle of PBS washing (as above). After drying, TSA dye was added to the circled area and incubated at room temperature for 10 min in the dark. Slides were then washed in TBST on a decolorizing shaker (5 min each).

To begin the second staining round, sections were placed in antigen retrieval buffer identical to the initial step and microwaved for 8 min at medium power and 7 min at medium-low power. After cooling, the second primary antibody was applied and incubated overnight at 4°C in a humidified chamber. Slides were then washed in PBS (as above), slightly dried, and incubated with corresponding fluorescent secondary antibody at room temperature for 50 min in the dark. The slides were again subjected to a PBS washing cycle (as above).

For nuclear counterstaining, DAPI solution was applied to the circled area and incubated at room temperature for 10 min in the dark. After washing in PBS (as above), autofluorescence was quenched by applying B-type quencher solution to the circled area for 5 min, followed by rinsing under running water for 10 min. This step was omitted if intrinsic fluorescence needed to be visualized. Finally, slides were mounted using anti-fluorescence quenching mounting medium and sealed with coverslips. Fluorescent signals were acquired using appropriate filters: DAPI (excitation 330–380 nm, emission 420 nm), 488 (excitation 465–495 nm, emission 515–555 nm), CY3 (excitation 510–560 nm, emission 590 nm), and CY5 (excitation 608–648 nm, emission 672–712 nm).

Transcriptional dynamics of renal cell types during kidney development

To characterize gene expression dynamics across developmental stages two comparison groups were established: fattening vs. weaning (FW) and maturity vs. weaning (MW). Differential expression was performed independently for each group using the Wilcoxon rank-sum test implemented in the "scanpy.tl.rank_genes_groups" function. Comparisons were made within the same cell type—for example, proximal tubule (PT) cells from the FW and MW stages. Differentially expressed genes (DEGs) were considered significantly up-regulated if they had a log fold change greater than 0.25 and an adjusted *P* value less than 0.05 and were considered significantly down-regulated if they had a log fold change less than −0.25 and an adjusted *P* value less than 0.05. Overlapping up-regulated and down-regulated genes between the FW and MW groups were then identified. These overlapping gene sets were subjected to pathway enrichment analysis to reveal shared developmental regulatory programs.

Heterogeneity of PT cells across developmental stages and breeds

PT cells were extracted from the filtered dataset. The "NormalizeData" function from the Seurat R package was used for normalization, and 800 highly variable genes were selected using the "FindVariableFeatures" function. Experimental batch effect correction was performed using "FindIntegrationAnchors" and "IntegrateData". The integrated data were scaled using the "ScaleData function", followed by dimensionality reduction using "RunPCA". UMAP embedding was computed using the top 30 PCs via "RunUMAP", and clustering was conducted using the "FindNeighbors" and "FindClusters" functions (resolution=0.05). This analysis identified five transcriptionally distinct PT subtypes.

PT pseudo-cell construction

To reduce noise and assess aggregate expression patterns, pseudo-cells were generated for each PT subtype. Single cells were randomly grouped in sets of 50, and the expression matrix for each pseudo-cell was calculated by averaging the gene expression profiles of the constituent cells.

Weighted gene coexpression network analysis (WGCNA)

Pseudo-cells generated from each PT subtype were merged for downstream analysis. Gene filtering was performed using OGFSC (v.0.2.3) (Hao et al., 2019) with the following parameters: plot_option=1, nBins=30, minBinSize=100, LR_p=0.01, alpha=0.5, and TW_threshold=0.0001. Subsequently, the filtered gene expression matrix was subjected to WGCNA (v.1.72.1) (Langfelder & Horvath, 2008) to identify modules of co-expressed genes.

Pathway enrichment analysis

Functional enrichment analysis was conducted using the ClueGO plugin (v.2.5.10) (Bindea et al., 2009) in Cytoscape. Multiple testing correction was applied using the Benjamini-Hochberg method. Terms with an adjusted *P* value below 0.05 were considered significantly enriched.

Comparison of PC cells between BMX and WB at the same developmental stage

PC cells were independently collected from BMX and WB kidneys during the weaning and maturity periods. Raw count matrices were normalized and log-transformed using the "scanpy.pp.normalize_total" and "scanpy.pp.log1p" functions in Python. The top 2 000 highly variable genes were selected using "scanpy.pp.highly_variable", and PCA was performed using "scanpy.tl.pca". Data integration was carried out using Harmony (v.0.0.9) (Korsunsky et al., 2019) to eliminate batch effects across samples. Dimensionality reduction and clustering were performed using "scanpy.tl.umap" and "scanpy.tl.louvain", with resolution set to 0.2 for the weaning period and 0.1 for the maturity period. Pathway enrichment analysis was subsequently performed on the top 300 DEGs for each identified PC cell subtype in both stages.

Cell-cell communication analysis

Intercellular signaling networks were inferred using CellChat (v.1.6.1) in R (Jin et al., 2021) based on known ligand-receptor interactions. Analysis was performed separately for each sample. Cell types represented by fewer than 30 cells in a given sample were excluded from the analysis.

RESULTS

Dynamic single-nucleus transcriptomic profiling during kidney development in BMX and WB

To characterize transcriptomic dynamics during porcine kidney development, snRNA-seq was performed on eight samples spanning three developmental stages: weaning (postnatal days 30 and 42), fattening (postnatal days 150), and maturity (postnatal days 730 and 774). These included five samples from BMX and three from WB (Figure 1A). After stringent quality control, 71 081 high-quality nuclei were retained, with a median of 2 146 genes detected per nucleus (Supplementary Table S1).

Data integration across breeds was performed using the "FindIntegrationAnchors" and "IntegrateData" functions in

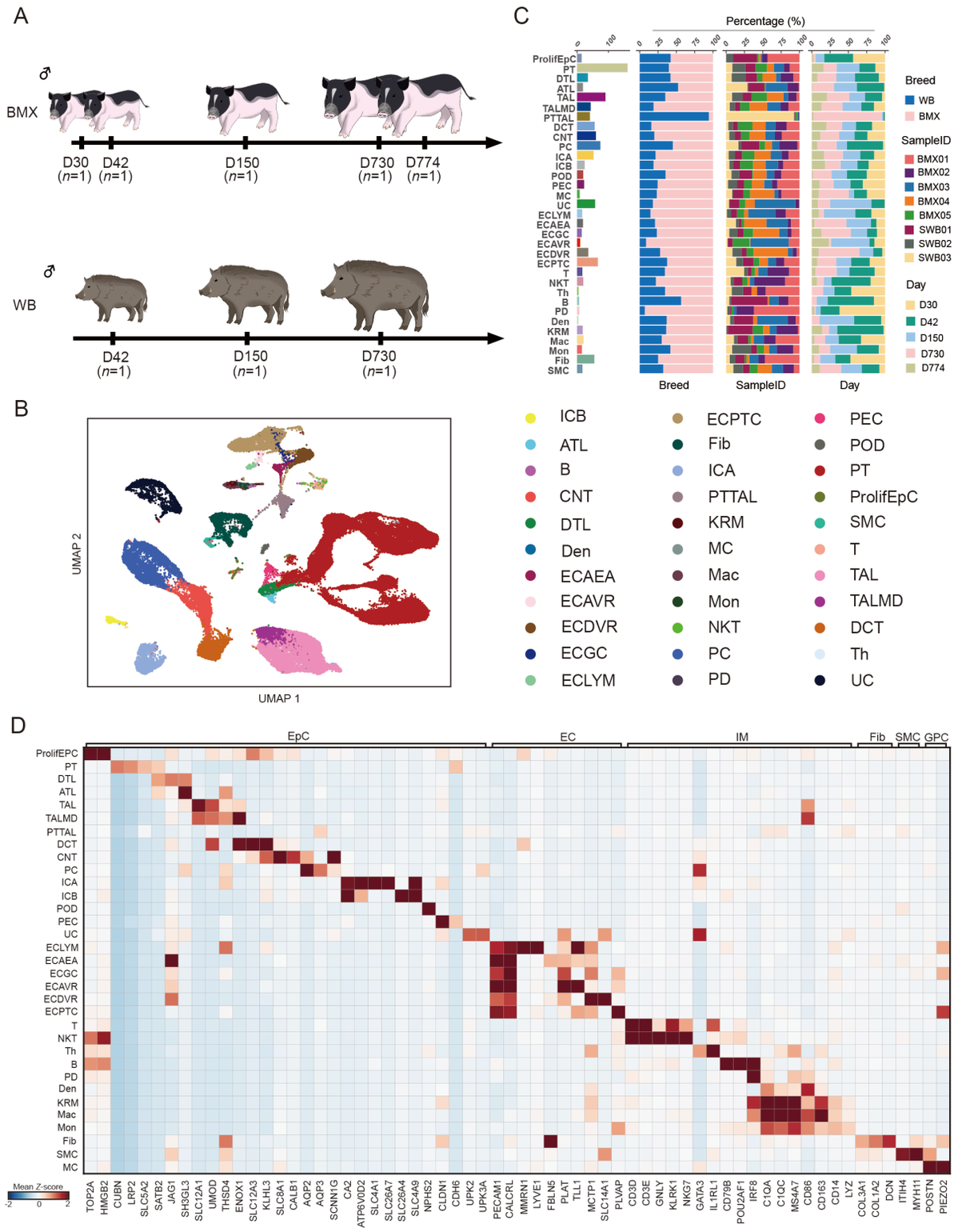

Figure 1 Single-nucleus RNA sequencing reveals renal cell composition across developmental stages and pig breeds

A: Schematic overview of experimental workflow. B: UMAP visualization of 71 081 high-quality nuclei from eight samples representing two pig breeds (BMX and WB) across three developmental stages, annotated by 33 distinct cell types: proliferative epithelial cells (ProlifEpC), proximal tubule (PT), descending thin limb (DTL), ascending thin limb (ATL), thick ascending limb (TAL), thick ascending limb (macula densa) (TALMD), proximal tubule/thick ascending limb (PTTAL), distal convoluted tubule (DCT), connecting tubule (CNT), principal cell (PC), intercalated cell type A (ICA), intercalated cell type B (ICB), podocyte (POD), parietal epithelial cell (PEC), urothelial cell (UC), lymphatic endothelial cell (ECLYM), afferent/efferent arteriole (ECAEA), glomerular endothelium (ECGC), ascending vasa recta (ECAVR), descending vasa recta of endothelial cell (ECDVR), peritubular capillaries of endothelial cell (ECPTC), T cell (T), natural killer T cell (NKT), T helper cells (Th), B cell (B), plasmacytoid dendritic (PD), kidney residual macrophage (KRM), macrophage (Mac), monocytes (Mon), fibroblast (Fib), smooth muscle cell (SMC), mesangial cell (MC). C: Bar plots showing, from left to right, number of nuclei, breed distribution, sample distribution, and postnatal day distribution for each cell type. D: Heatmap of representative marker genes used to define 33 identified cell types.

Seurat. Seven major cell types were identified, including EpCs, ProlifEpCs, ECs, IMs, Fibs, SMCs, and GPCs. Subtype annotation of EpC, EC, and IM populations was further refined using Harmony, based on canonical marker genes retrieved from published datasets (Franzén et al., 2019; Uhlén et al., 2015). Together, this approach enabled high-resolution identification of 33 distinct cell types (Figure 1B–D).

Annotation accuracy was validated using published reference datasets (Lake et al., 2023; Miao et al., 2021; Stewart et al., 2019). Cross-dataset prediction using the 'FindIntegrationAnchors' and 'TransferData' functions yielded high correspondence with known kidney cell types (Supplementary Figure S1A–D).

Transcriptional dynamics and heterogeneity of renal cell types during kidney development

To elucidate transcriptional changes in porcine kidney cell types during postnatal development, differential gene expression analysis was performed in the FW and MW groups separately. Notably, PT, PC, and TAL cells exhibited the highest number of DEGs in both comparisons, with greater magnitude observed in the MW group (Figure 2A, B; Supplementary Table S2), indicating substantial transcriptional remodeling during late developmental stages.

In PT cells, 1 600 genes were consistently up-regulated in both FW and MW groups (Figure 2C; Supplementary Table S2). These genes were significantly enriched in pathways related to cellular macromolecule metabolism, organic substance catabolism, lipid metabolism, transmembrane transport, ion channel regulation, positive regulation of glucose transmembrane transport, and long-chain fatty acid import across the plasma membrane (Figure 2D), indicating that PT cells primarily support ion and nutrient transport and metabolic activity during later development. In contrast, 808 genes were down-regulated in both groups (Figure 2C; Supplementary Table S2), with enrichment in kidney and renal system development, regulation of growth and developmental processes, tube morphogenesis, and kidney epithelial development (Figure 2D), suggesting that PT cells are primarily involved in maintaining cell growth and development during the weaning period. Additionally, ProlifEpCs with elevated G2M scores were identified (Figure 2E), predominantly observed during the weaning period across both breeds (Figure 2F). Refined cell-type annotation revealed coordinated proliferation across multiple renal epithelial subtypes during this critical developmental window (Figure 2G, H).

Heterogeneity of PT cells across developmental stages and breeds

Given the extensive transcriptional shifts in PT cells, their heterogeneity was further characterized across developmental stages and breeds. PT cells play a major role in fluid-electrolyte homeostasis and acid-base equilibrium by reabsorbing 60%–70% of filtered water and sodium chloride, along with a majority of sodium bicarbonate (Chrysopoulou & Rinschen, 2024; Curthoys & Moe, 2014; Fuchs & Wolf, 2023; Nakhoul & Batuman, 2011; Zhuo & Li, 2013). A total of 25 797 PT cells were re-clustered using the "FindIntegrationAnchors" and "IntegrateData" functions in Seurat (Figure 3A). Pseudo-cells were constructed from every 50 PT cells, followed by WGCNA (Langfelder & Horvath, 2008). Enrichment analysis of module genes revealed functional distinctions among PT subtypes (Supplementary Table S3). PT3, primarily derived from the weaning and fattening periods (Figure 3B), was associated with a yellow module involved in metal ion transmembrane transporter activity (*KCNN2* and *SLC39A8*), active transmembrane transporter activity, and sodium ion transport (*SLC4A8*) (Figure 3C, D). PT0, PT2, and PT4 were enriched for a red module involved in organic acid transport (*SLC16A2* and *SLC16A3*), amino acid transmembrane transport (*SLC7A2* and *SLC38A6*), and vitamin transport (*SCARB1*) (Figure 3C, D). PT1, present during the fattening and maturity periods (Figure 3B), was enriched in a brown module linked to hormone metabolism (*HSD17B6*) and long-chain fatty acid metabolism (*ELOVL6*) (Figure 3C, D). Notably, PT2 was almost exclusively derived from the WB breed at maturity (Figure 3B) and enriched in a turquoise module involved in regulation of immune system processes (*GRN*, *IL1RAP*, *LGALS3*, *MIF*, and *STAT3*), response to wounding (*GPX1* and *HIF1A*), and response to hypoxia (*HIF1A*) (Figure 3C, D). This immune-enriched profile was corroborated in an independent mature WB sample, in which PT cells exhibited elevated expression of immune-related genes (*GRN*, *MIF*, and *GPX1*) (Figure 3E, F), consistent with the transcriptional features of PT2. MetaNeighbor analysis further supported the reproducibility of this PT2 subtype, demonstrating strong similarity scores across replicates (Figure 3G) (Crow et al., 2018).

Heterogeneity of PCs across breeds at the same developmental stages

PCs play essential roles in renal fluid and electrolyte homeostasis via key transporters, including epithelial sodium channel(*SCNN1A*, *SCNN1B*, and *SCNN1G*) for sodium reabsorption, Renal outer medullary potassium channel(*KCNJ1*) for potassium secretion, and apical water channel aquaporin-2 (AQP2) for water reabsorption, with basolateral aquaporins AQP3 and AQP4 facilitating transcellular water movement (Pearce et al., 2015).

To investigate PC heterogeneity across pig breeds, PCs were separately extracted from BMX and WB breeds at the weaning and maturity periods. During the weaning period, three distinct PC subtypes were identified (Figure 4A). PC0, shared by both breeds, showed elevated expression of *AQP2*, *AQP3*, *SCNN1A*, *SCNN1B*, *SCNN1G*, and *KCNJ1* (Figure 4C), along with high expression of ureteric bud-associated markers *CDH16* and *ELF*3 (Figure 4C). Enrichment analysis revealed activation of pathways associated with ureteric bud development, BMP signaling pathway, kidney epithelial development, and morphogenesis of a branching epithelium (Figure 4B) indicating shared maturation processes in both breeds.

Two breed-specific PC subtypes were also identified. BMX-derived PC1 was primarily associated with ATP metabolic processes, aerobic respiration, and oxidative phosphorylation (Figure 4B), with high expression of *ATP6*, *COX1*, *CYTB*, *ND1*, and *ND5* (Figure 4C). In contrast, WB-derived PC2 was enriched in temperature homeostasis and cold-induced thermogenesis (Figure 4B), with high expression of *IGF1R*, *JAK2*, and *ZNF516* (Figure 4C), likely reflecting an adaptive response to environmental temperature fluctuations during early development.

At the maturity stage, PC heterogeneity was more pronounced (Figure 4D), particularly in metabolic specialization. BMX-specific PC0 was enriched in aerobic metabolism, including aerobic respiration and oxidative

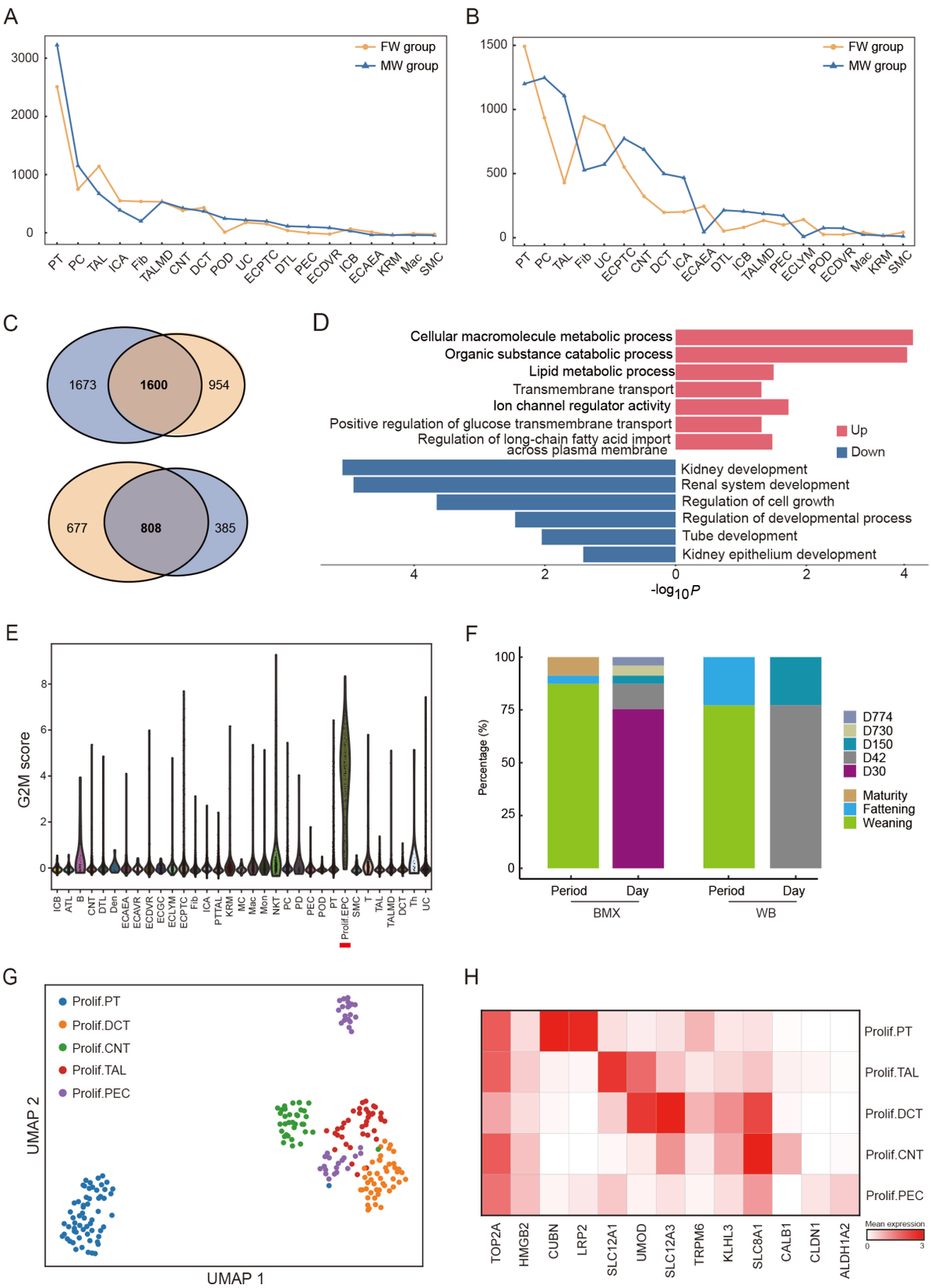

Figure 2 Transcriptional dynamics of renal cell populations during kidney development

A: Number of up-regulated differentially expressed genes (DEGs) in each cell type in FW and MW groups. B: Number of down-regulated DEGs in each cell type in FW and MW groups. C: Overlap of up-regulated (top) and down-regulated (bottom) DEGs between FW and MW groups. D: Bar plot showing enriched pathways associated with overlapping up-regulated and down-regulated DEGs in PT cells. E: Violin plot showing G2M scores across all cell types, with proliferating epithelial cells exhibiting the highest scores. F: Bar plot showing postnatal day and developmental period contributions to ProlifEpCs in BMX and WB pigs. G: UMAP visualization of all ProlifEpC nuclei, colored by five proliferating epithelial subtypes. H: Heatmap of representative marker genes for each proliferating epithelial subtype.

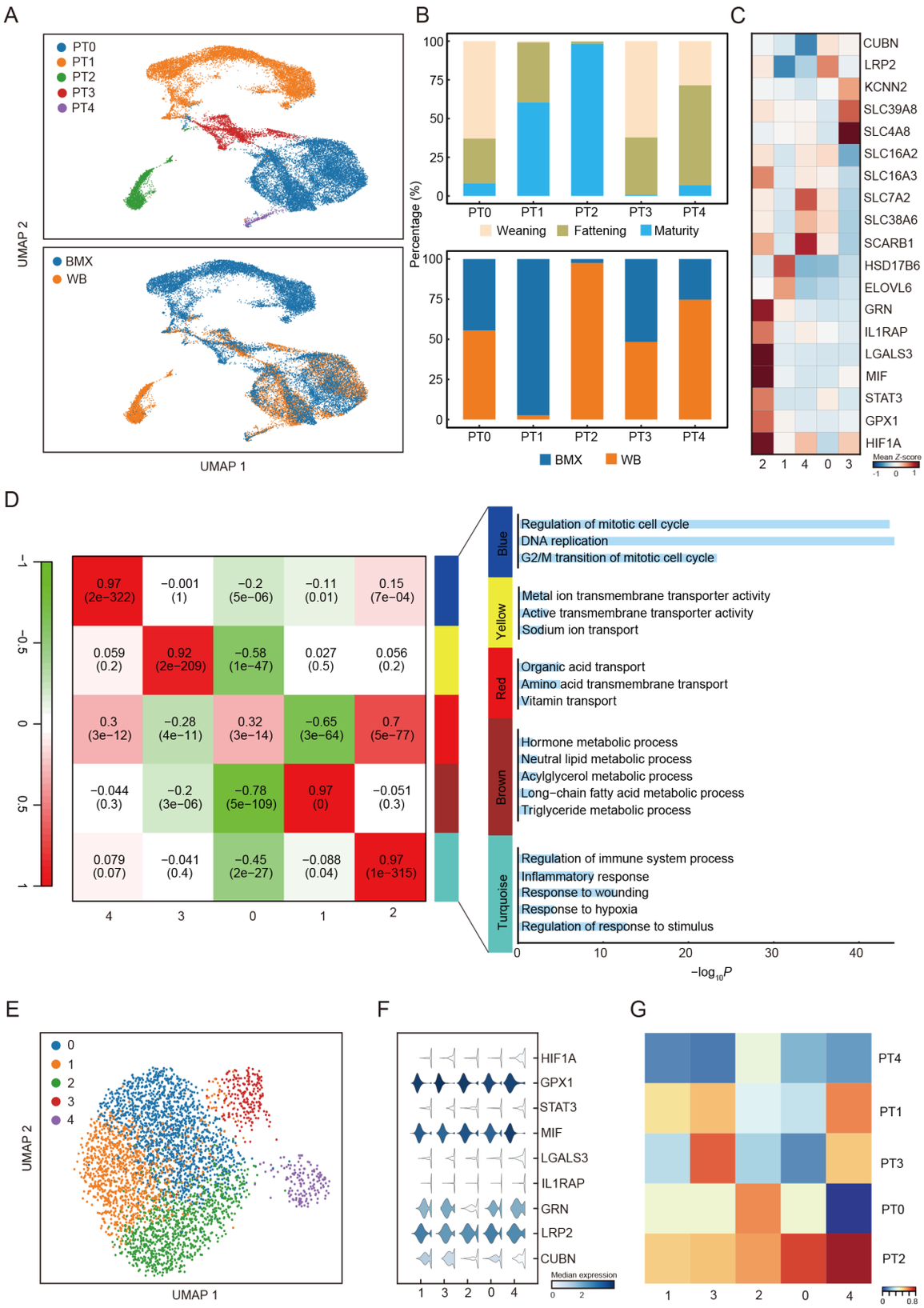

Figure 3 Heterogeneity of PT cells across developmental stages and pig breeds

A: UMAP visualization of PT cells, colored by five identified PT subtypes (top) and by breed (down). B: Bar plots showing contributions of developmental periods (top) and breeds (bottom) to each PT subtype. C: Heatmap of representative marker gene expression across PT subtypes. D: Left: Heatmap of WGCNA modules significantly correlated with PT subtypes. Right: Bar plots of enriched pathways associated with each WGCNA module. E: UMAP visualization of PT cells from an independent mature WB sample, colored by five PT subtypes. F: Violin plot showing expression of representative marker genes across PT subtypes in an independent mature WB sample. G: Heatmap showing transcriptional similarity between PT subtypes identified in an independent mature WB sample and those shown in A.

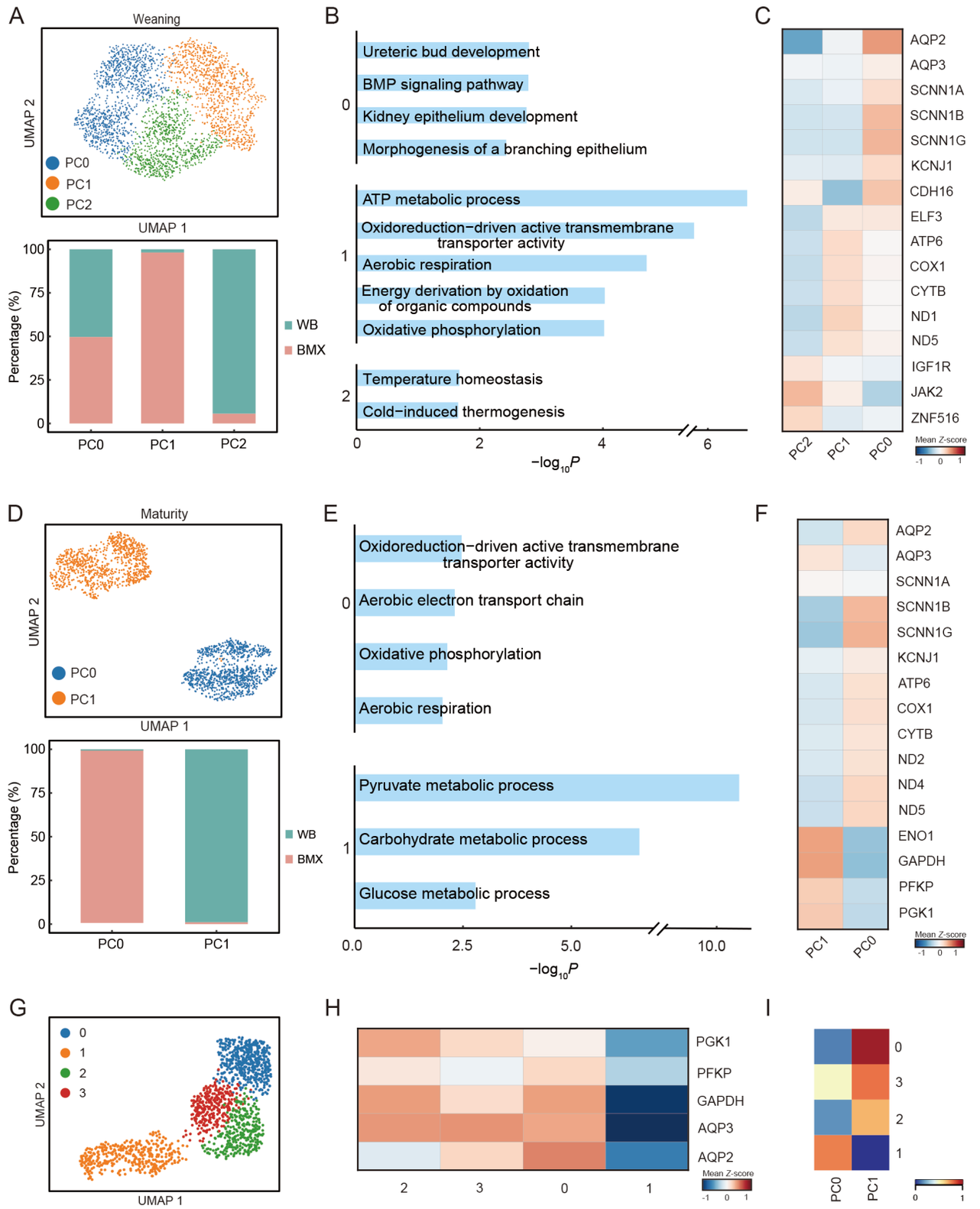

Figure 4 Heterogeneity of PC populations across breeds within the same developmental periods

A: UMAP visualization of PCs at the weaning period colored by three PC subtypes (top) and bar plot of breed contributions to each subtype (bottom). B: Bar plot of enriched pathways associated with top 300 differentially expressed genes (DEGs) in each PC subtype at the weaning period. C: Heatmap of representative marker gene expression across PC subtypes at the weaning period. D: UMAP visualization of PCs at the maturity period colored by three PC subtypes (top) and bar plot of breed contributions to each subtype (bottom). E: Bar plot of enriched pathways associated with top 300 DEGs in each PC subtype at the maturity period. F: Heatmap of representative marker gene expression across PC subtypes at the maturity period. G: UMAP visualization of PCs from an independent mature WB sample, colored by four PC subtypes. H: Heatmap of representative marker gene expression across PC subtypes in an independent mature WB sample. I: Heatmap of transcriptional similarity between PC subtypes identified in an independent mature WB sample and those shown in D.

phosphorylation (Figure 4E), reflecting adaptation to sustained energy demands through efficient oxygen utilization. In contrast, WB-specific PC1 showed high expression of genes (*GAPDH*, *PFKP*, and *PGK1*) (Figure 4F) involved in carbohydrate and glucose metabolism (Figure 4E), suggesting a metabolic shift favoring rapid energy mobilization for adaptive response in natural environments.

Consistent patterns were observed in an independent mature WB sample, where multiple PC subtypes (PC0, PC2, and PC3) exhibited elevated expression of genes involved in carbohydrate and glucose metabolism (*GAPDH*, *PFKP*, and *PGK1*) (Figure 4G, H). MetaNeighbor analysis further supported the transcriptional similarity between these subtypes and the WB-specific PC1 cluster (Figure 4I).

Cell-type-specific epidermal growth factor (EGF) signaling patterns during kidney development

To elucidate intercellular communication during kidney development, CellChat analysis was conducted for each sample. Among all signaling pathways, EGF signaling exhibited the highest overall communication strength throughout the developmental stages in BMX pigs (Figure 5A; Supplementary Figure S2A–J). The EGF/EGFR axis regulates diverse biological processes, including cellular proliferation, growth, and metabolic activity (Barberán & Cebrià, 2019; Orofiamma et al., 2022). Detailed analysis of the EGF signaling network revealed subtype-specific ligand-receptor interactions across renal epithelial lineages. Specifically, betacellulin (BTC) was predominantly secreted by ATL, DTL, ICA, and PC cells and engaged receptor complexes including EGFR, ERBB4, ERBB2-ERBB4, and EGFR-ERBB2. EGF expression was localized in PT, TAL, TALMD, and DCT cells, targeting EGFR and EGFR-ERBB2, while transforming growth factor-α (TGF-α) was specifically secreted by UC cells, targeting EGFR and EGFR-ERBB2 (Figure 5B; Supplementary Figure S3A–E). Gene expression profiling confirmed the cell-type-specific expression of these ligands (Figure 5C).

Immunofluorescence staining of paraffin sections further validated the developmental expression of EGF in PT cells across the three developmental periods (Figure 5D–F; Supplementary Figure S4A–C), and TGF-α in UC cells at the weaning stage (Figure 5G; Supplementary Figure S4D). These findings suggest that different epithelial subtypes participate in EGF-mediated signaling via distinct ligand-receptor pairs, likely contributing to their specialized roles in renal maturation and homeostasis.

DISCUSSION

Kidney development progresses through two distinct stages. The initial stage involves reciprocal inductive signaling between the ureteric bud and metanephric mesenchyme, establishing the foundational branching architecture. In the subsequent stage, tubular epithelial cells within the subcapsular nephrogenic zone undergo rapid proliferation to expand nephron populations (Gossens & Unsworth, 1972; Saxen, 1987). At birth, mammalian kidneys remain functionally immature, exhibiting limited glomerular filtration, inefficient sodium reabsorption, and reduced urinary concentrating capacity (Velarde et al., 1995). These deficiencies persist beyond weaning, with full functional maturation occurring by six weeks in rats and by approximately 18 months in humans (Aperia & Celsi, 1992; Rane et al., 1985). Postnatal kidney maturation entails region-specific structural remodeling, including sustained proliferation and differentiation in the cortex, zonation of the medulla into inner and outer compartments, and extracellular matrix (ECM) reorganization surrounding collecting ducts in medullary and papillary regions (Márquez et al., 2002).

Among nephron components, PT, PC, and TAL cells exhibited pronounced transcriptional reprogramming from weaning to maturity. These dynamic changes likely reflect the establishment of complex solute transport systems and regulatory machinery required for full physiological competence. PT cells, predominantly located in the renal cortex, mediate the bulk of reabsorption, reclaiming water, electrolytes, and nutrients from glomerular filtrate to preserve systemic homeostasis (Chrysopoulou & Rinschen, 2024; Curthoys & Moe, 2014; Fuchs & Wolf, 2023; Nakhoul & Batuman, 2011; Zhuo & Li, 2013). In the current study, PT cells shifted from development-related functions during weaning to metabolic and transport functions during fattening and maturity. To elucidate the molecular basis of this functional diversification, PT cells were subdivided into transcriptionally defined subtypes, followed by pseudo-cell construction and WGCNA. Despite the limited number of pseudo-cells per subtype, this approach reduced transcriptomic noise and delineated core functional modules. Distinct subtypes exhibited specific enrichment patterns: PT3 was primarily involved in ion transport, PT0 and PT4 were linked to organic acid transport, and PT1 was associated with fatty acid metabolism. Additionally, a unique PT2 subtype enriched in immune-related functions emerged exclusively in mature WB, which may represent an adaptive response to environmental pathogen exposure encountered by feral populations, in contrast to the more controlled and managed conditions of domesticated pig rearing systems. (Chen et al., 2013; Hühr et al., 2020; Meng et al., 2009).

WB inhabiting anthropogenically altered landscapes are primarily nocturnal, exhibiting increased activity during cold nighttime periods (Keuling et al., 2008; Ohashi et al., 2013; Podgórski et al., 2013; Russo et al., 1997). Unlike many mammalian neonates, piglets lack brown adipose tissue and depend predominantly on shivering thermogenesis for heat production (Trayhurn et al., 1989). However, recent findings suggest the existence of an alternative thermogenic mechanism that compensates for the absence of brown fat/UCP1 thermogenesis, enabling WB to tolerate cold environments (Zhang et al., 2025). Transcriptomic evidence supports this adaptation, as a WB-specific PC2 subtype was enriched in pathways related to thermoregulation and cold-induced thermogenesis during the weaning period, including *IGF1R*, *JAK2*, and *ZNF516* signaling. In addition, WB demonstrate superior physical endurance supported by enhanced glycolysis and anaerobic metabolism (He et al., 2017). Consistent with this metabolic phenotype, the PC1 subtype at maturity showed elevated expression of *GAPDH*, *PFKP*, and *PGK1*, genes associated with carbohydrate and glucose metabolism, suggesting efficient energy mobilization under environmental stress.

The EGF/EGFR signaling pathway plays crucial roles in cellular proliferation, growth, and metabolic regulation (Barberán & Cebrià, 2019; Orofiamma et al., 2022). Cellular interaction analysis revealed cell-type-specific ligand-receptor pairing patterns within the EGF pathway across epithelial subtypes. EGF, the canonical ligand with the highest affinity

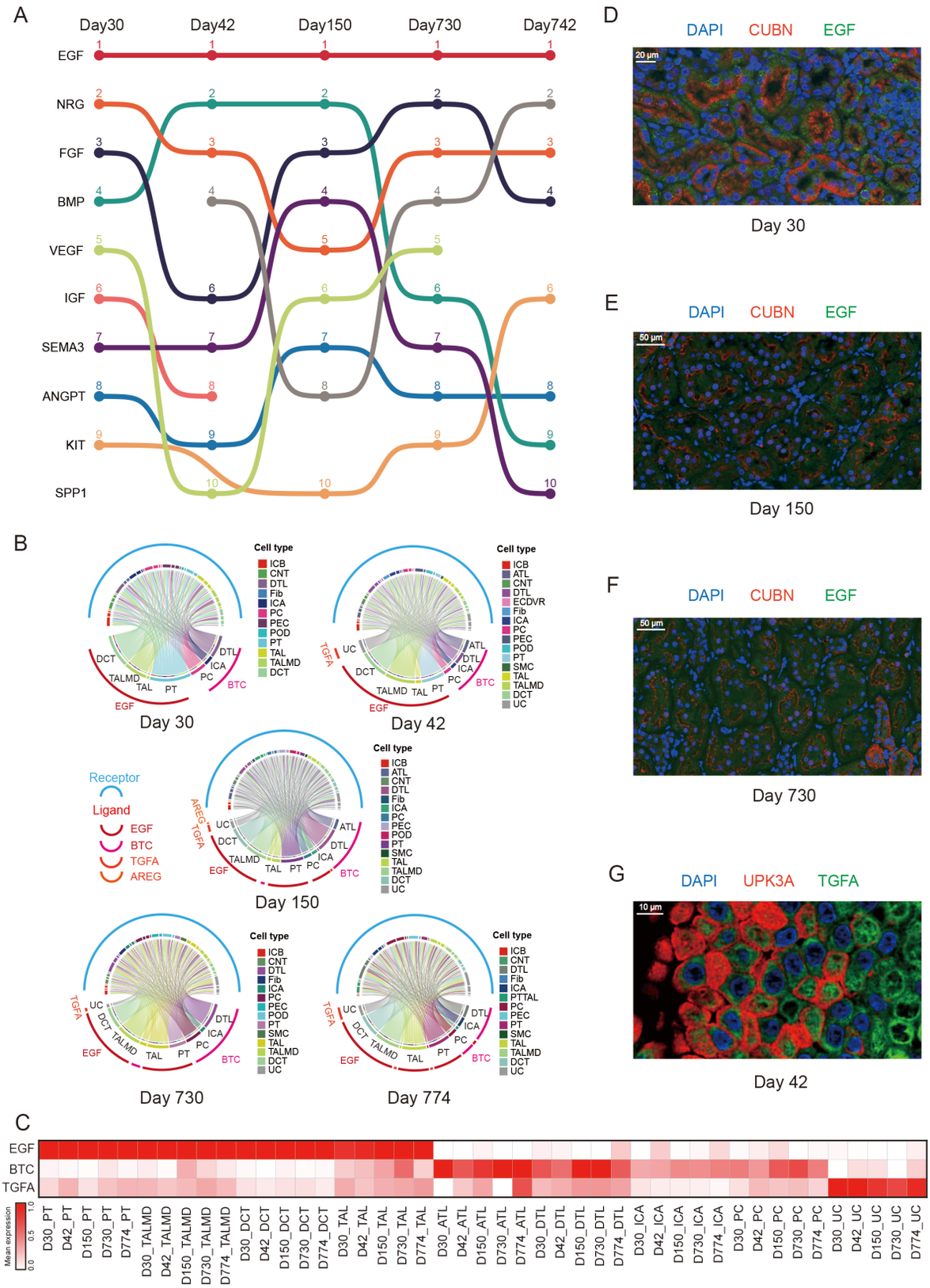

Figure 5 Distinct epithelial tubule subtypes utilize specific EGF ligands for intercellular signaling

A: Bump chart showing ranked signal strength of cell-cell interactions across postnatal timepoints in BMX pig kidneys. B: Chord diagram showing EGF pathway interactions between ligand-expressing and target epithelial cell types at each postnatal timepoint in BMX pigs. C: Dot plot showing expression of EGF family ligands (EGF, BTC, TGF-α) across kidney epithelial cell types during postnatal development in BMX pigs. D–F: Immunofluorescence double staining of BMX pig kidney sections showing EGF (green), CUBN (red), and DAPI (blue) antibodies at postnatal days 30 (D), 150 (E), and 730 (F). Scale bars: 20 μm, 50 μm, and 50 μm, respectively. G: Immunofluorescence double staining of BMX pig kidney section showing TGF-α (green), UPK3A (red), and DAPI (blue) antibodies at postnatal day 42. Scale bar: 10 μm.

for EGFR, was initially discovered in submaxillary gland extracts (Cohen, 1960). The kidney is a primary source of EGF production, and elevated urinary EGF concentrations have been identified as an independent risk factor for chronic kidney disease progression (Carpenter & Cohen, 1979; Dvorak, 2010; Fisher et al., 1989; Nojiri et al., 2012; Rayego-Mateos et al., 2018; Read et al., 1984). EGF contributes to renal physiology and pathology by modulating sodium and magnesium transport through various ion channels (Mroz & Keely, 2012; O'Mahony et al., 2008; Trinh et al., 2008; Zheleznova et al., 2011), promoting tubular epithelial proliferation (Coaxum et al., 2014; Zepeda-Orozco et al., 2017), and participating in polycystic kidney disease pathogenesis (Gattone II et al., 1995; Ryan et al., 2010; Veizis & Cotton, 2005) and post-ischemic regeneration (Gomella et al., 1989; Laouari et al., 2011). In this study, EGF was primarily expressed in PT, TAL, TALMD, and DCT cells, where it engaged EGFR and EGFR-ERBB2 complexes, consistent with previous findings (Rayego-Mateos et al., 2018).

BTC, a member of the EGF ligand family of ErbB receptor tyrosine kinases, is likely to be important in neonatal development (Dunbar & Goddard, 2000; Dunbar et al., 1999). Similar to EGF and TGFA, BTC promotes proliferation of fibroblasts, smooth muscle and epithelial cells(Nagaoka et al., 2008). In the present analysis, BTC was primarily secreted by ATL, DTL, ICA and PC subtypes, engaging EGFR, ERBB4, ERBB2-ERBB4, and EGFR-ERBB2 receptor complexes. TGF-α, which is structurally and functionally similar to EGF, is expressed in normal adult human kidneys and has been implicated in renal fibrogenesis (Gomella et al., 1989; Huovila et al., 2005). Results showed that TGF-α was specifically expressed in UCs, targeting EGFR and EGFR-ERBB2. Prior *in vitro* studies have reported that recombinant TGF-α up-regulates proinflammatory gene expression in cultured tubular epithelial cells. Given the susceptibility of UCs to noxious stimuli due to their direct exposure to pathogens, toxins, and urinary irritants (Arrighi, 2015; Birder & Andersson, 2013; Dalghi et al., 2020), TGF-α secretion from UCs may act via EGFR signaling to mediate urothelial-tubular communication and contribute to inflammatory modulation during kidney inflammation.

This study revealed period- and breed-dependent divergence among renal cell populations, with pronounced differences in metabolic regulation, immune responses, and intercellular signaling. Progressive development was accompanied by systematic enhancement of cellular metabolic capacity, whereas breed-specific transcriptional programs highlighted distinct strategies in energy metabolism and immune modulation, features that may influence graft adaptation and functional stability following transplantation. In addition, cell-type-specific engagement of EGF signaling suggested a contributory role in regulating proliferative and regenerative potential within donor kidneys. Together, these findings provide valuable insights to inform period-specific donor selection and functional evaluation frameworks for kidney xenotransplantation. However, the relatively small sample size may limit the generalizability of our conclusions. Therefore, future studies with larger cohorts are warranted to validate and expand upon these observations, laying a solid foundation for more refined and personalized xenotransplantation strategies.

DATA AVAILABILITY

Raw sequencing data were deposited in the GSA database (accession number CRA023987), NCBI database (BioProjectID PRJNA1332661), and Science Data Bank database (https://doi.org/10.57760/sciencedb.j00139.00262)

SUPPLEMENTARY DATA

Supplementary data to this article can be found online.

COMPETING INTERESTS

The authors declare that they have no competing interests.

AUTHORS' CONTRIBUTIONS

T.X.Y. was responsible for data quality control and analysis. T.X.Y. wrote the original draft. T.X.Y., Y.Z., and S.Y.Y. reviewed and revised the manuscript. T.X.Y., Y.Z., X.Y.C, T.L., and Y.L. were involved in experimental validation. All authors read and approved the final version of the manuscript.

ACKNOWLEDGEMENTS

We thank Lu-Sheng Huang for conceptualizing, designing, and supervising the project and Ying Su for preparing the antibodies for sequential double immunofluorescence staining of paraffin sections.

REFERENCES

Alpern RJ, Caplan MJ, Moe OW. 2012. Seldin and Giebisch's The Kidney: Physiology and Pathophysiology. 5th ed. Amsterdam: Elsevier.

Aperia A, Celsi G. 1992. Ontogenic processes in nephron epithelia. *In*: Seldin DW, Giebisch G. The Kidney: Physiology and Pathophysiology. New York: Raven Press, 803–828.

Arrighi S. 2015. The urothelium: anatomy, review of the literature, perspectives for veterinary medicine. *Annals of Anatomy - Anatomischer Anzeiger*, **198**: 73–82.

Balzer MS, Rohacs T, Susztak K. 2022. How many cell types are in the kidney and what do they do?. *Annual Review of Physiology*, **84**: 507–531.

Barberán S, Cebrià F. 2019. The role of the EGFR signaling pathway in stem cell differentiation during planarian regeneration and homeostasis. *Seminars in Cell & Developmental Biology*, **87**: 45–57.

Bindea G, Mlecnik B, Hackl H, et al. 2009. ClueGO: a Cytoscape plug-in to decipher functionally grouped gene ontology and pathway annotation networks. *Bioinformatics*, **25**(8): 1091–1093.

Birder L, Andersson KE. 2013. Urothelial signaling. *Physiological Reviews*, **93**(2): 653–680.

Bolhuis JE, Schouten WGP, Schrama JW, et al. 2006. Effects of rearing and housing environment on behaviour and performance of pigs with different coping characteristics. *Applied Animal Behaviour Science*, **101**(1-2): 68–85.

Carpenter G, Cohen S. 1979. Epidermal growth factor. *Annual Review of Biochemistry*, **48**(1): 193–216.

Chen SY, Gomes R, Costa V, et al. 2013. How immunogenetically different are domestic pigs from wild boars: a perspective from single-nucleotide polymorphisms of 19 immunity-related candidate genes. *Immunogenetics*, **65**(10): 737–748.

Chrysopoulou M, Rinschen MM. 2024. Metabolic rewiring and communication: an integrative view of kidney proximal tubule function. *Annual Review of Physiology*, **86**(1): 405–427.

Coaxum SD, Blanton MG, Joyner A, et al. 2014. Epidermal growth factor-induced proliferation of collecting duct cells from Oak Ridge polycystic kidney mice involves activation of Na^+/H^+ exchanger. *American Journal of Physiology-Cell Physiology*, **307**(6): C554–C560.

Cohen J. 2025(2025-04-11). Exclusive: longest human transplant of pig kidney fails. American Association for the Advancement of Science,

https://www.science.org/content/article/longest-human-transplant-pig-kidney-fails.

Cohen S. 1960. Purification of a nerve-growth promoting protein from the mouse salivary gland and its neuro-cytotoxic antiserum. *Proceedings of the National Academy of Sciences of the United States of America*, **46**(3): 302–311.

Collier RJ, Beede DK, Thatcher WW, et al. 1982. Influences of environment and its modification on dairy animal health and production. *Journal of Dairy Science*, **65**(11): 2213–2227.

Crow M, Paul A, Ballouz S, et al. 2018. Characterizing the replicability of cell types defined by single cell RNA-sequencing data using MetaNeighbor. *Nature Communications*, **9**(1): 884.

Curthoys NP, Moe OW. 2014. Proximal tubule function and response to acidosis. *Clinical Journal of the American Society of Nephrology*, **9**(9): 1627–1638.

Dalghi MG, Montalbetti N, Carattino MD, et al. 2020. The urothelium: life in a liquid environment. *Physiological Reviews*, **100**(4): 1621–1705.

Dunbar AJ, Goddard C. 2000. Structure-function and biological role of betacellulin. *The International Journal of Biochemistry & Cell Biology*, **32**(8): 805–815.

Dunbar AJ, Priebe IK, Belford DA, et al. 1999. Identification of betacellulin as a major peptide growth factor in milk: purification, characterization and molecular cloning of bovine betacellulin. *Biochemical Journal*, **344 Pt 3**(Pt 3): 713–721.

Dvorak B. 2010. Milk epidermal growth factor and gut protection. *The Journal of Pediatrics*, **156**(2 Suppl): S31–S35.

El-Achkar TM, Eadon MT, Menon R, et al. 2021. A multimodal and integrated approach to interrogate human kidney biopsies with rigor and reproducibility: guidelines from the Kidney Precision Medicine Project. *Physiological Genomics*, **53**(1): 1–11.

Fisher DA, Salido EC, Barajas L. 1989. Epidermal growth factor and the kidney. *Annual Review of Physiology*, **51**(1): 67–80.

Fleming SJ, Chaffin MD, Arduini A, et al. 2023. Unsupervised removal of systematic background noise from droplet-based single-cell experiments using CellBender. *Nature Methods*, **20**(9): 1323–1335.

Franzén O, Gan LM, Björkegren JLM. 2019. PanglaoDB: a web server for exploration of mouse and human single-cell RNA sequencing data. *Database*, **2019**: baz046.

Fuchs MAA, Wolf M. 2023. Renal proximal tubule cells: power and finesse. *The Journal of Clinical Investigation*, **133**(9): e169607.

Gattone II VH, Lowden DA, Cowley BD, Jr. 1995. Epidermal growth factor ameliorates autosomal recessive polycystic kidney disease in mice. *Developmental Biology*, **169**(2): 504–510.

Gomella LG, Sargent ER, Wade TP, et al. 1989. Expression of transforming growth factor alpha in normal human adult kidney and enhanced expression of transforming growth factors alpha and beta 1 in renal cell carcinoma. *Cancer Research*, **49**(24 Pt 1): 6972–6975.

Gossens CL, Unsworth BR. 1972. Evidence for a two-step mechanism operating during *in vitro* mouse kidney tubulogenesis. *Development*, **28**(3): 615–631.

Guyton AC, Hall JE. 2005. Textbook of Medical Physiology. 11th ed. Philadelphia: Elsevier Saunders.

Hao J, Cao W, Huang J, et al. 2019. Optimal Gene Filtering for Single-Cell data (OGFSC) —a gene filtering algorithm for single-cell RNA-seq data. *Bioinformatics*, **35**(15): 2602–2609.

Hao YH, Hao S, Andersen-Nissen E, et al. 2021. Integrated analysis of multimodal single-cell data. *Cell*, **184**(13): 3573–3587. E29.

He DF, Ma JD, Long KR, et al. 2017. Differential expression of genes related to glucose metabolism in domesticated pigs and wild boar. *Bioscience, Biotechnology, and Biochemistry*, **81**(8): 1478–1483.

Huovila APJ, Turner AJ, Pelto-Huikko M, et al. 2005. Shedding light on ADAM metalloproteinases. *Trends in Biochemical Sciences*, **30**(7): 413–422.

Hühr J, Schäfer A, Schwaiger T, et al. 2020. Impaired T-cell responses in domestic pigs and wild boar upon infection with a highly virulent African swine fever virus strain. *Transboundary and Emerging Diseases*, **67**(6): 3016–3032.

Jin SQ, Guerrero-Juarez CF, Zhang LH, et al. 2021. Inference and analysis of cell-cell communication using CellChat. *Nature Communications*, **12**(1): 1088.

Johnson RJ, Stenvinkel P, Jensen T, et al. 2016. Metabolic and kidney diseases in the setting of climate change, water shortage, and survival factors. *Journal of the American Society of Nephrology*, **27**(8): 2247–2256.

Keuling O, Stier N, Roth M. 2008. How does hunting influence activity and spatial usage in wild boar *Sus scrofa* L. ?. *European Journal of Wildlife Research*, **54**(4): 729–737.

Kojima M, Degawa M. 2022. Sex, organ, and breed differences in the mRNA expression of drug transporters in the liver and kidney of pigs. *Biological and Pharmaceutical Bulletin*, **45**(4): 508–516.

Korsunsky I, Millard N, Fan J, et al. 2019. Fast, sensitive and accurate integration of single-cell data with Harmony. *Nature Methods*, **16**(12): 1289–1296.

Kshirsagar AV, Zeitler EM, Weaver A, et al. 2022. Environmental exposures and kidney disease. *Kidney360*, **3**(12): 2174–2182.

Lake BB, Menon R, Winfree S, et al. 2023. An atlas of healthy and injured cell states and niches in the human kidney. *Nature*, **619**(7970): 585–594.

Langfelder P, Horvath S. 2008. WGCNA: an R package for weighted correlation network analysis. *BMC Bioinformatics*, **9**(1): 559.

Laouari D, Burtin M, Phelep A, et al. 2011. TGF-α mediates genetic susceptibility to chronic kidney disease. *Journal of the American Society of Nephrology*, **22**(2): 327–335.

Lobacz MA, Sullivan M, Mellor D, et al. 2012. Effect of breed, age, weight and gender on radiographic renal size in the dog. *Veterinary Radiology & Ultrasound*, **53**(4): 437–441.

Lunney JK, Van Goor A, Walker KE, et al. 2021. Importance of the pig as a human biomedical model. *Science Translational Medicine*, **13**(621): eabd5758.

Márquez MG, Cabrera I, Serrano DJ, et al. 2002. Cell proliferation and morphometric changes in the rat kidney during postnatal development. *Anatomy and Embryology*, **205**(5-6): 431–440.

Mass General Brigham Communications. 2024(2024-03-21). In a first, genetically edited pig kidney is transplanted into human. Mass General Brigham Communications, https://hms.harvard.edu/news/first-genetically-edited-pig-kidney-transplanted-human.

Meng XJ, Lindsay DS, Sriranganathan N. 2009. Wild boars as sources for infectious diseases in livestock and humans. *Philosophical Transactions of the Royal Society B: Biological Sciences*, **364**(1530): 2697–2707.

Miao J, Zhu HH, Wang JN, et al. 2024. Experimental models for preclinical research in kidney disease. *Zoological Research*, **45**(5): 1161–1174.

Miao Z, Balzer MS, Ma ZY, et al. 2021. Single cell regulatory landscape of the mouse kidney highlights cellular differentiation programs and disease targets. *Nature Communications*, **12**(1): 2277.

Mroz MS, Keely SJ. 2012. Epidermal growth factor chronically upregulates Ca^{2+}-dependent Cl^- conductance and TMEM16A expression in intestinal epithelial cells. *The Journal of Physiology*, **590**(8): 1907–1920.

Nagaoka T, Fukuda T, Hashizume T, et al. 2008. A betacellulin mutant promotes differentiation of pancreatic acinar AR42J cells into insulin-producing cells with low affinity of binding to ErbB1. *Journal of Molecular Biology*, **380**(1): 83–94.

Nakhoul N, Batuman V. 2011. Role of proximal tubules in the pathogenesis of kidney disease. *In*: Herrera GA. Experimental Models for Renal Diseases: Pathogenesis and Diagnosis. S. Karger AG.

Nojiri T, Yoshizato T, Fukami T, et al. 2012. Clinical significance of amphiregulin and epidermal growth factor in colostrum. *Archives of Gynecology and Obstetrics*, **286**(3): 643–647.

Ohashi H, Saito M, Horie R, et al. 2013. Differences in the activity pattern of the wild boar *Sus scrofa* related to human disturbance. *European Journal of Wildlife Research*, **59**(2): 167–177.

O'Mahony F, Toumi F, Mroz MS, et al. 2008. Induction of $Na^+/K^+/2Cl^-$ cotransporter expression mediates chronic potentiation of intestinal epithelial Cl^- secretion by EGF. *American Journal of Physiology-Cell Physiology*, **294**(6): C1362–C1370.

Orofiamma LA, Vural D, Antonescu CN. 2022. Control of cell metabolism by the epidermal growth factor receptor. *Biochimica et Biophysica Acta (BBA) - Molecular Cell Research*, **1869**(12): 119359.

Pearce D, Soundararajan R, Trimpert C, et al. 2015. Collecting duct principal cell transport processes and their regulation. *Clinical Journal of the American Society of Nephrology*, **10**(1): 135–146.

Podgórski T, Baś G, Jędrzejewska B, et al. 2013. Spatiotemporal behavioral plasticity of wild boar (*Sus scrofa*) under contrasting conditions of human pressure: primeval forest and metropolitan area. *Journal of Mammalogy*, **94**(1): 109–119.

Qin F, Zou S. 2025(2025-03-14). Pig kidney transplanted into renal disease patient. China Daily, https://www.chinadaily.com.cn/a/202503/14/WS67d380b4a310c240449dab8e.html.

Rane S, Aperia A, Eneroth P, et al. 1985. Development of urinary concentrating capacity in weaning rats. *Pediatric Research*, **19**(5): 472–475.

Rayego-Mateos S, Rodrigues-Diez R, Morgado-Pascual JL, et al. 2018. Role of epidermal growth factor receptor (EGFR) and its ligands in kidney inflammation and damage. *Mediators of Inflammation*, **2018**(1): 8739473.

Read LC, Upton FM, Francis GL, et al. 1984. Changes in the growth-promoting activity of human milk during lactation. *Pediatric Research*, **18**(2): 133–139.

Russo L, Massei G, Genov PV. 1997. Daily home range and activity of wild boar in a Mediterranean area free from hunting. *Ethology Ecology & Evolution*, **9**(3): 287–294.

Ryan S, Verghese S, Cianciola NL, et al. 2010. Autosomal recessive polycystic kidney disease epithelial cell model reveals multiple basolateral epidermal growth factor receptor sorting pathways. *Molecular Biology of the Cell*, **21**(15): 2732–2745.

Saxen L. 1987. Organogenesis of the Kidney. Cambridge: Cambridge University Press.

Stewart BJ, Ferdinand JR, Young MD, et al. 2019. Spatiotemporal immune zonation of the human kidney. *Science*, **365**(6460): 1461–1466.

Timoneda O, Balcells I, Núñez JI, et al. 2013. miRNA expression profile analysis in kidney of different porcine breeds. *PLoS One*, **8**(1): e55402.

Trayhurn P, Temple NJ, Aerde JV. 1989. Evidence from immunoblotting studies on uncoupling protein that brown adipose tissue is not present in the domestic pig. *Canadian Journal of Physiology and Pharmacology*, **67**(12): 1480–1485.

Trinh NTN, Privé A, Maillé E, et al. 2008. EGF and K^+ channel activity control normal and cystic fibrosis bronchial epithelia repair. *American Journal of Physiology-Lung Cellular and Molecular Physiology*, **295**(5): L866–L880.

Uhlén M, Fagerberg L, Hallström BM, et al. 2015. Tissue-based map of the human proteome. *Science*, **347**(6220): 1260419.

Veizis IE, Cotton CU. 2005. Abnormal EGF-dependent regulation of sodium absorption in ARPKD collecting duct cells. *American Journal of Physiology-Renal Physiology*, **288**(3): F474–F482.

Velarde V, Humphreys J, Vio CP, et al. 1995. Postnatal maturation of tissue kallikrein-producing cells (connecting tubule cells) in the rat kidney: a morphometric and immunohistochemical study. *Anatomy and Embryology*, **192**(5): 407–414.

Wolf FA, Angerer P, Theis FJ. 2018. SCANPY: large-scale single-cell gene expression data analysis. *Genome Biology*, **19**(1): 15.

Wolock SL, Lopez R, Klein AM. 2019. Scrublet: computational identification of cell doublets in single-cell transcriptomic data. *Cell Systems*, **8**(4): 281–291. E9.

Yao TX, Li N, Huang LS. 2025. Integrated single-cell transcriptomic map of pig kidney cells across various periods and anatomical sites. *Zoological Research*, **46**(2): 469–482.

Zepeda-Orozco D, Wen HM, Hamilton BA, et al. 2017. EGF regulation of proximal tubule cell proliferation and VEGF-A secretion. *Physiological Reports*, **5**(18): e13453.

Zhang MP, Traspov A, Yang JW, et al. 2025. Genomic and transcriptomic insights into vitamin A-induced thermogenesis and gene reuse as a cold adaptation strategy in wild boars. *Communications Biology*, **8**(1): 116.

Zheleznova NN, Wilson PD, Staruschenko A. 2011. Epidermal growth factor-mediated proliferation and sodium transport in normal and PKD epithelial cells. *Biochimica et Biophysica Acta (BBA) - Molecular Basis of Disease*, **1812**(10): 1301–1313.

Zheng GXY, Terry JM, Belgrader P, et al. 2017. Massively parallel digital transcriptional profiling of single cells. *Nature Communications*, **8**(1): 14049.

Zhuo JL, Li XC. 2013. Proximal nephron. *Comprehensive Physiology*, **3**(3): 1079–1123.